

Millikelvin-resolved ambient thermography

Kechao Tang^{1,2*}, Kaichen Dong^{1,2†}, Christopher J. Nicolai³, Ying Li^{4#}, Jiachen Li^{1,2}, Shuai Lou¹, Cheng-Wei Qiu⁴, David H. Raulet³, Jie Yao^{1,2}, Junqiao Wu^{1,2§}

Thermography detects surface temperature and subsurface thermal activity of an object based on the Stefan-Boltzmann law. Impacts of the technology would be more far-reaching with finer thermal sensitivity, called noise-equivalent differential temperature (NEDT). Existing efforts to advance NEDT are all focused on improving registration of radiation signals with better cameras, driving the number close to the end of the roadmap at 20 to 40 mK. In this work, we take a distinct approach of sensitizing surface radiation against minute temperature variation of the object. The emissivity of the thermal imaging sensitizer (TIS) rises abruptly at a preprogrammed temperature, driven by a metal-insulator transition in cooperation with photonic resonance in the structure. The NEDT is refined by over 15 times with the TIS to achieve single-digit millikelvin resolution near room temperature, empowering ambient thermography for a broad range of applications such as in operando electronics analysis and early cancer screening.

INTRODUCTION

The Stefan-Boltzmann law states that the surface of conventional materials at temperature T emits infrared (IR) radiation with the radiated power (P_{rad}) proportional to T^4 (1). By calibrating the received P_{rad} using the T^4 law, IR cameras image the temperature distribution on an object. The IR thermography at ambient finds diverse applications in fields ranging from night vision (2), security surveillance (3), and electronics inspection (4) to medical diagnostics (5), structural defect screening (6), and academic research (7). The noise-equivalent differential temperature (NEDT), one key figure of merit for these cameras, has been improved via better designs to enhance detection and conversion of P_{rad} (8–10), while assuming the T dependence of P_{rad} to be strictly bounded by the T^4 law. Consequently, the roadmap of NEDT currently saturates at 20 to 40 mK for uncooled bolometers, with little advance in the past decades (1, 11). In this work, in contrast, we turn to a distinct approach of lifting the limitation of the T^4 law to improve NEDT by more than an order of magnitude (figs. S1 and S2). The IR camera generates the temperature reading (T_{IR}) by assuming a constant wavelength-integrated emissivity (ε_0) for the object. In the case when the actual emissivity (ε) is different from ε_0 , T_{IR} deviates from the actual temperature T via $P_{\text{rad}} = \varepsilon_0 \sigma T_{\text{IR}}^4 = \varepsilon \sigma T^4$, where $\sigma = \frac{2\pi^5 k_B^4}{15 c^2 h^3}$ is the Stefan-Boltzmann constant. The differentiation of T_{IR} over T is

$$\frac{dT_{\text{IR}}}{dT} = \left(\frac{\varepsilon}{\varepsilon_0} \right)^{1/4} \left(1 + \frac{1}{4} \frac{d\ln\varepsilon}{d\ln T} \right) \quad (1)$$

and is assumed to be equal to $(\varepsilon/\varepsilon_0)^{1/4}$ as ε of conventional materials is nearly T -independent (12). However, dT_{IR}/dT would be much

higher if ε becomes strongly dependent on T , drastically amplifying small variations in T . In this work, the strong, positive T dependence of ε is realized by integrating the metal-insulator transition (MIT) of tungsten-doped vanadium dioxide ($W_xV_{1-x}O_2$) with a photonic cavity structure (Fig. 1A). ε switches to a much higher value when T rises above the transition temperature, boosting dT_{IR}/dT and refining NEDT by a factor over 15 (Fig. 1B). The device, coined as a thermal imaging sensitizer (TIS), is fabricated on a thin flexible substrate and can be conveniently and repeatedly applied to and peeled off from the object surface, as shown in Figs. 1A and 2A.

RESULTS

The function of TIS builds on the well-known MIT (13) of the strongly correlated electron material $W_xV_{1-x}O_2$ at the temperature $T_{\text{MIT}} \approx 67^\circ\text{C} - 24^\circ\text{C} \cdot x \cdot 100$, which can be conveniently tuned from 67° to -100°C by varying the composition x (14, 15). In the insulating (I) state, the material is basically transparent to IR in the 8- to 14 μm wavelength range (16, 17), and incoming IR radiation will penetrate through the top two layers with negligible absorption and reflected by the Ag mirror, as shown in Fig. 1A. In contrast, when the $W_xV_{1-x}O_2$ switches to the metallic (M) state, it becomes highly absorptive to IR radiation (16, 17), and the absorption is further enhanced by the photonic resonance around wavelength of 9.8 μm in the designed 1/4-wavelength cavity. Consequently, the system will go through an abrupt increase in absorbance (A) and hence emissivity, according to the Kirchhoff's law of radiation (18).

The sensitizing function of TIS is first characterized by imaging from an IR camera. Figure 2C plots T_{IR} as a function of T in the upper panel, called the sensitizing property curve (SPC), for three selected TIS's with W fractions of 1.5, 1.3, and 1.1%. These samples exhibit sharp increase in T_{IR} at $T \sim 28^\circ$, 34° , and 39°C , respectively, corresponding to the designed T_{MIT} of the $W_xV_{1-x}O_2$ layer. Because T_{MIT} can be pre-set by the W fraction x , and the T_{MIT} of TIS, along with its working temperature range, can be precisely designed to fit various applications.

The high dT_{IR}/dT enables drastic improvement of NEDT when taking IR images of objects coated with TIS, removing the artificial step features on the temperature profile while preserving good fidelity (fig. S9). The power of TIS is further demonstrated by the "Rayleigh

Copyright © 2020
The Authors, some
rights reserved;
exclusive licensee
American Association
for the Advancement
of Science. No claim to
original U.S. Government
Works. Distributed
under a Creative
Commons Attribution
NonCommercial
License 4.0 (CC BY-NC).

¹Department of Materials Science and Engineering, University of California, Berkeley, Berkeley, CA 94720, USA. ²Division of Materials Sciences, Lawrence Berkeley National Laboratory, Berkeley, CA 94720, USA. ³Department of Molecular and Cell Biology, University of California, Berkeley, Berkeley, CA 94720, USA. ⁴Department of Electrical and Computer Engineering, National University of Singapore, Singapore 117583, Singapore.

*Present address: Key Laboratory of Microelectronic Devices and Circuits (MOE), Institute of Microelectronics, Peking University, Beijing 100871, P. R. China.

†These authors contribute equally to the work.

#Present address: Interdisciplinary Center for Quantum Instrumentation, College of Information Science and Electronic Engineering, Zhejiang University, Hangzhou 310027, China.

§Corresponding author. Email: wuj@berkeley.edu

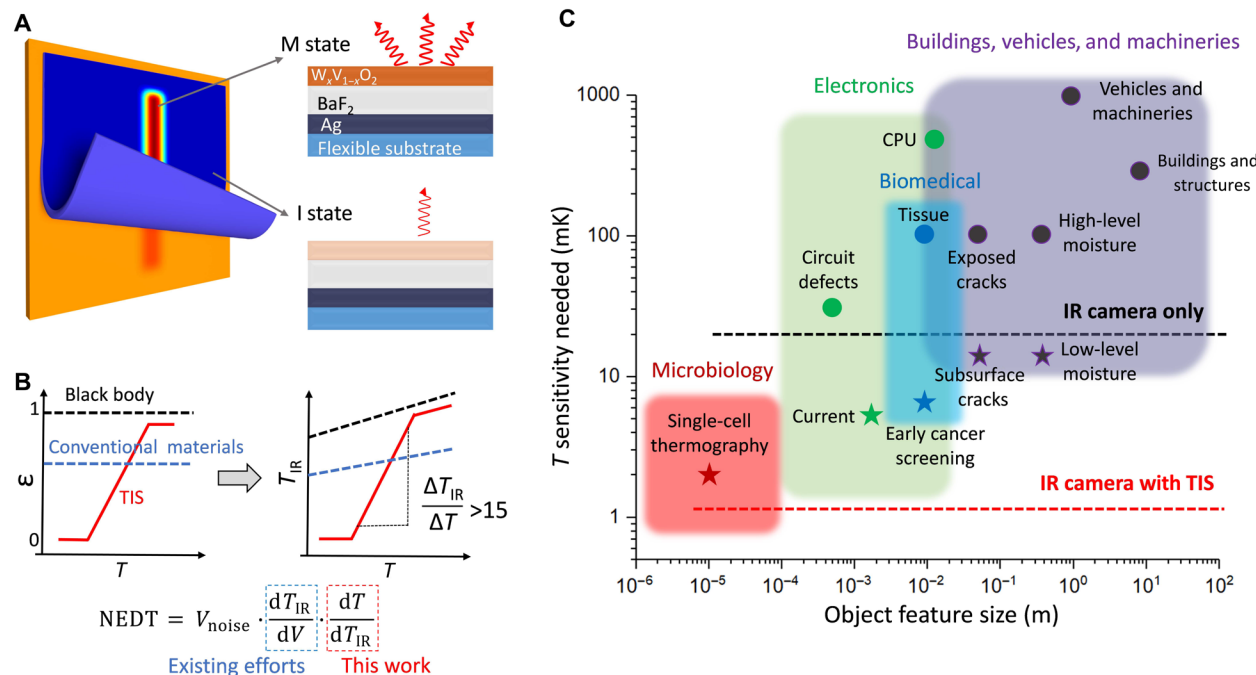


Fig. 1. Thermal imaging sensitized by MIT. (A) Schematic illustration of boosted temperature resolution of thermography by the thermal imaging sensitizer (TIS) and its working mechanism. As the object (covered with TIS) is heated up across the MIT, the TIS switches from a reflector (hence, low absorbance and low emissivity) in the insulating (I) phase to a resonator (hence, high absorbance and high emissivity) in the metallic (M) phase for mid-IR waves. (B) In contrast to conventional materials or black body, the sharp increase in thermal emissivity (ϵ) at the MIT of $W_xV_{1-x}O_2$ introduces a high amplification (>15) of ΔT to ΔT_{IR} and thus reduction in NEDT. (C) Representative temperature resolution required for ambient thermography in various applications with paradigmatic feature sizes (details in the Supplementary Materials). TIS pushes boundaries of these applications and generates new markets.

Downloaded from https://www.science.org on February 26, 2025

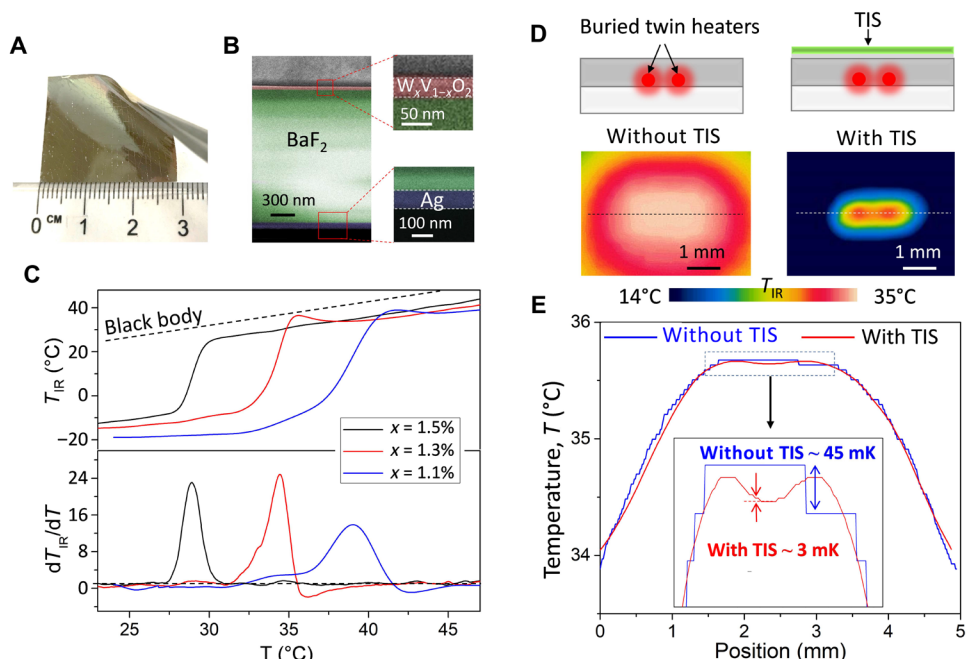


Fig. 2. Characterization of the TIS. (A) Optical image of a fabricated TIS, showing high flexibility. (B) False-colored cross section of the TIS film imaged by scanning electron microscopy (SEM) before transfer. (C) IR temperature and temperature amplification as a function of actual temperature for TIS with three selected compositions (fractions of W in the $W_xV_{1-x}O_2$ layer). (D) Schematics and directly captured IR images of two closely placed (1-mm gap) small heaters imaged without and with TIS. (E) Calibrated temperature profiles along the dashed lines in (D). The twin-heater feature is distinctly resolved in the TIS-assisted imaging because of the ~15 times improvement of the experimental thermal sensitivity. Photo credit: Kechao Tang, University of California, Berkeley.

criterion”-like experiment in Fig. 2D. Here, two small heaters were placed close to each other on a substrate. When imaged with a conventional IR camera, the twin-heater thermal feature cannot be resolved, whereas they become clearly distinguishable when imaged with the TIS coating. Note that for TIS-assisted IR imaging, T_{IR} recorded is not the actual temperature (T), but it could be readily calibrated back to T (Fig. 2E) using the SPC in Fig. 2C (details in Materials and Methods).

The substantial reduction in NEDT greatly benefits thermal imaging of electronics (19–21). Ultrasensitive passive thermal imaging can probe the operation status of electronic devices and is especially useful for scenarios where lock-in amplification is not available. The over 15 times sensitization enables accurate detection of very weak thermal features in electronic circuits (details in the Supplementary Materials). The TIS-assisted thermal imaging engenders a new technology that we call in operando electronics analysis (oEA). The oEA extends the application of thermography from inspecting defective devices to normal devices in operation. By analyzing extremely weak thermal features on the surface of the device, oEA noninvasively “spies” on and reveals the working mode of the device in real time. Figure 3A demonstrates thermographic differentiation of distinct workloads and operation modes of a central processing unit (CPU). The various input algorithms cause slightly different power generation and temperature patterns on the surface of the CPU, which are readily resolved with the TIS-assisted thermography.

The oEA is further extended from qualitative probing to quantitative extraction of electronic operation parameters, such as electrical current flowing in wires and circuit traces (Fig. 3B). By calibrating local temperature rise from the joule heating, the current levels in the circuit traces can be evaluated thermographically at high accuracy without interrogation with current meters. The operation can be performed simultaneously for multiple, adjacent traces on a circuit board, allowing noninvasive and quantitative current mapping. On the basis of thermal profiles calibrated with different currents in a single trace, the currents flowing in multiple traces on the printed circuit board (PCB) are quantitatively determined with high accuracy (Fig. 3C; details in figs. S13 to S15).

The TIS also empowers groundbreaking advance in medical thermography (5). Thermography is broadly applied in areas such as cancer detection (22), diagnosis of diabetic neuropathy and vascular disorder (23), fever screening (24), dental care (25), and surgery (26). Breast cancer, for example, can be detected by IR cameras because hypervascularity in the tumors leads to slightly abnormal local temperature. With the advantages in cost, accessibility, and noninvasiveness, thermography is used to screen breast cancer before mammography testing (27). However, current medical thermography suffers from the low diagnostic sensitivity and specificity (28), while TIS-assisted thermography would reduce noise, improve thermographic fidelity, and enable cancer screening at earlier stages, potentially improving the survival rate of patients (29).

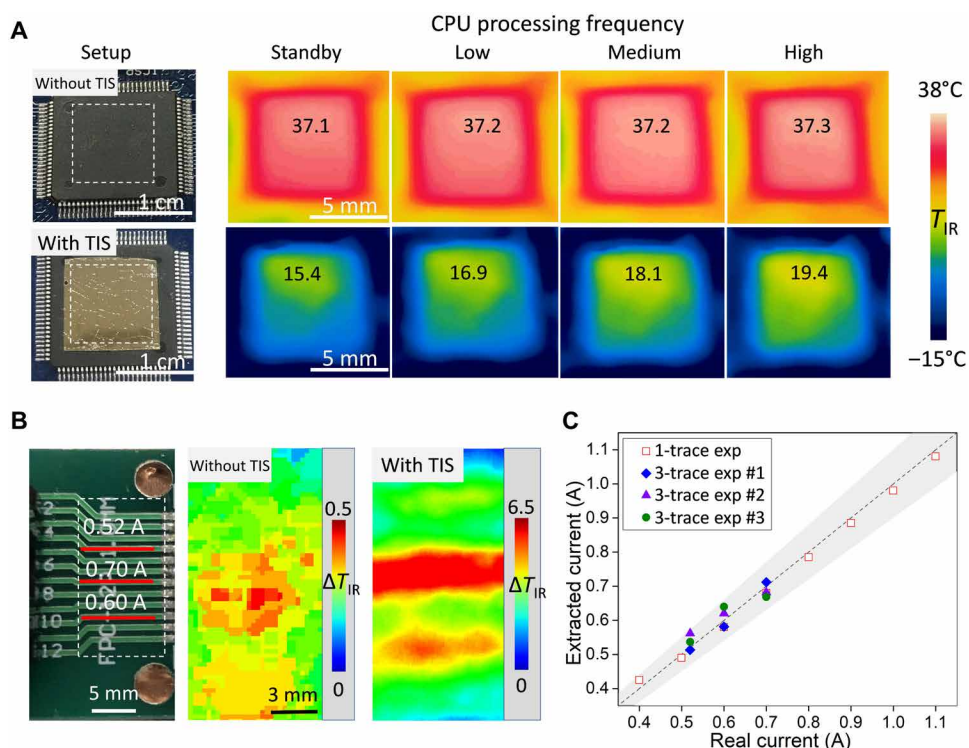


Fig. 3. TIS applied to oEA. (A) Enhancement of thermographic contrast on a central processing unit (CPU) by TIS, allowing differentiation of various working modes. (B) Optical and IR mappings of temperature rise because of currents flowing in adjacent circuit traces on a printed circuit board (PCB), imaged without and with TIS. (C) Extracted current versus real current in the traces. The dashed line and the shadow correspond to the ideal current extraction and $\pm 10\%$ deviation, respectively. The experimental error bars for the data points are comparable to the size of the points. The model used to extract currents is detailed in the Supplementary Materials. Photo credit: Kechao Tang, University of California, Berkeley.

We demonstrate the benefit of TIS in subcutaneous cancer screening by tracking the growth of malignant tumors in mice. Figure 4A shows the schematic of the experiment and the picture of a laboratory mouse. RMA cells, belonging to the lymphoma cell line, were injected at two near spots on the mouse belly to initiate the tumor growth. On different days after the injection, an optical image, an IR image without TIS, and an IR image with TIS were taken to characterize the tumor (Fig. 4B). On day 3 after the cell injection, no features were detected in the optical or conventional IR imaging, while cold spots at the two tumors were clearly captured in the TIS-assisted IR imaging. As the tumors grow larger on day 5, they could be barely observed visibly and by conventional IR imaging, while the IR imaging of the cold spots becomes much clearer and more confirmative with the TIS. On day 7, the tumors are large enough to be detected in all imaging methods, and the consistency of these features validates the TIS-assisted imaging in the early stage of the tumor. As we show in fig. S16, the benefit of TIS can be also extended to detecting other types of tumor cells, imaging the shape and size of tumors, and resolving multiple tumors when they are closely situated, similar to the scenario in Fig. 2E. The TIS can also be used in other medical thermography applications such as blood vessel imaging (fig. S17).

For broader applications in practical scenarios, TIS is also open to improvements in multiple prospects by future endeavors. For example, more delicate control in the W doping of VO_2 will allow for finer tuning of the working temperature to optimize performance for various conditions. Doping with other elements like Ga or Al may shift the working temperature above that of pristine VO_2 (67°C) to enable applications at higher temperature. Future engineering efforts to improve the quality of $\text{W}_x\text{V}_{1-x}\text{O}_2$ can improve the sharpness of MIT and the reduction in NEDT, further boosting the performance in sensitivity and resolution. Last, the response time of the device could be shortened by reducing the thickness of the flexible substrate film and improving the thermal contact with the target surface.

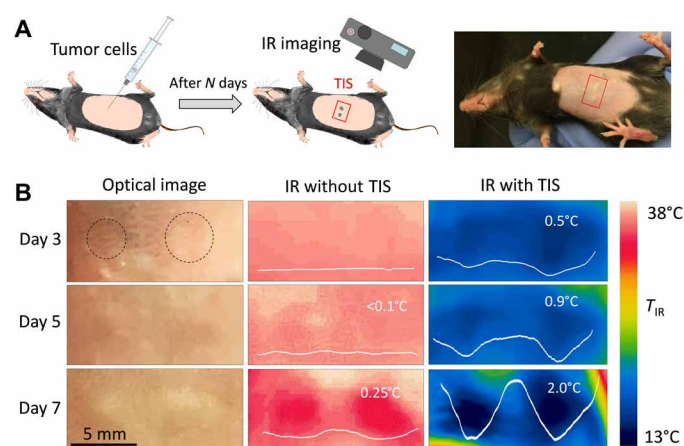


Fig. 4. TIS applied to medical thermography. (A) RMA cells were injected at two adjacent spots to initiate the tumor growth in mice, which was then tracked by optical imaging, IR imaging without TIS, and with TIS. (B) TIS imaging reveals the two tumors in early stage after the injection when they are not yet detectable visibly or by conventional thermography. The white curves are temperature profiles across the center of the two tumors in each IR image, labeled with the amplitude of T_{IR} variation in each curve. Photo credit: Kechao Tang, University of California, Berkeley.

DISCUSSION

Integrating the thermally driven metal-insulator phase transition with a resonant photonic structure, we innovate ambient thermography by drastically refining the temperature sensitivity to single digits of millikelvin. The TIS expands the applications of ambient thermography in electronics analysis and medical screening. As small temperature fluctuation exists over the surface of a wide range of objects and, in many cases, implicates unusual subsurface thermal activities, the TIS is envisioned to broadly affect many other fields (Fig. 1C). For example, at larger scales, the TIS-assisted thermography may be used to inspect, image, and monitor subsurface cracks and stressed spots in buildings and bridges (fig. S18) (30); at smaller scales, with the aid of high-resolution IR microscopy, the TIS may act as functional templates on which biological activities of cells and microbes can be thermally imaged in real time.

MATERIALS AND METHODS

Preparation of the TIS

$\text{W}_x\text{V}_{1-x}\text{O}_2$ thin films were grown on 170- μm -thick borosilicate glass substrates using pulse laser deposition (PLD). The PLD targets were prepared by mixing WO_3 and V_2O_5 powders with W:V atomic ratio ranging from 1.1 to 1.5%, and then made into 1-inch-diameter round discs with a hydraulic press. All thin films were deposited in 5 mtorr O_2 environment at 570°C substrate temperature, and the PLD laser energy was set at 321 mJ with 5-Hz pulse frequency. Thirty nanometers of $\text{W}_x\text{V}_{1-x}\text{O}_2$ was grown at a rate of 3 nm/min, followed by a postdeposition anneal at 570°C for 30 min in the same 5 mtorr O_2 environment. On top of the $\text{W}_x\text{V}_{1-x}\text{O}_2$ films, 1.5- μm -thick BaF_2 and 100-nm-thick Ag layers were grown sequentially via thermal evaporation. The growth rates of BaF_2 and Ag were controlled at 20 and 2 $\text{\AA}/\text{s}$, respectively. The thicknesses of the $\text{W}_x\text{V}_{1-x}\text{O}_2$, BaF_2 , and Ag layers were optimized for best optical performance with finite-element method simulation using COMSOL Multiphysics (fig. S4) and characterized by cross-sectional scanning electron microscopy (SEM) imaging.

In the transfer process, a piece of 0.06-mm-thick single-sided sticky scotch packaging tape was first carefully applied to fully cover the $\text{W}_x\text{V}_{1-x}\text{O}_2/\text{BaF}_2/\text{Ag}$ structure, where the Ag layer was stuck to the adhesive side without any residual air bubbles. The initial borosilicate glass substrate for thin-film growth was then etched off by 49% hydrofluoric acid in 5 min. After the release process, the scotch tape with transferred $\text{W}_x\text{V}_{1-x}\text{O}_2/\text{BaF}_2/\text{Ag}$ structure was rinsed in deionized water and dried with a N_2 gun. Detailed schematics and pictures of the process can be found in the fig. S5.

IR imaging and analysis

The IR images were captured by a FLIR ONE IR camera working at a wavelength range of 8 to 14 μm , with a frame rate of 8.7 Hz. To minimize the reflection signals from the camera and the surroundings, the default viewing angle was set as 15° instead of normal incident direction, and the experiments were performed either in an open-area, outdoor environment under clear sky (cloud free), or using a cold-plate setup. When doing experiments in outdoor environment, we avoid exposing the TIS and target surfaces to direct solar radiation, by setting up the system in the shadow of a building or blocking the sunlight with a solar shield. As described with more details in fig. S6, the cold-plate setup shows a similar effect comparable to experimenting in the outdoor environment.

When taking IR images, the camera measures the incident thermal radiation P_{rad} , and then gives the temperature reading (T_{IR}) assuming a constant emissivity for the target (e.g., $\epsilon_0 = 0.90$, default setting of the camera, which applies to all images in this work). T_{IR} was plotted as a function of the real temperature T to generate the SPC. The sharp increase in T_{IR} at MIT is consistent with emissivity measurement by Fourier transform IR spectroscopy (fig. S7) and defines a high slope of dT_{IR}/dT up to 25. This means that an object with tiny, unresolvable ΔT on the surface would become easily resolvable by normal IR cameras if the object is covered with the TIS. For instance, ΔT of 20 mK is never resolved by an IR camera whose NEDT is 45 mK. However, with the help of TIS, the same object will show up to 25 times higher ΔT_{IR} (500 mK) and is clearly resolved by the same IR camera.

Furthermore, the TIS is able to be applied to most near-ambient applications over the desired window of temperatures near T_{MIT} . Because T_{MIT} can be pre-set by the W fraction x , the T_{MIT} of TIS, along with its working temperature range, can be precisely designed to fit various applications. In addition, the angular independence of the SPC (fig. S8) and the mechanical flexibility allow TIS to be applied to nonflat, arbitrary surfaces with little impact to the performance.

All the IR images in the main figures show the map of T_{IR} , which represent thermal features of the object but is numerically different from a map of T in the case of imaging with TIS. A map of T can be readily converted from the above T_{IR} image using the SPC data: At each pixel of the image, by matching the T_{IR} with SPC in Fig. 2C, the actual temperature T can be obtained. Note that this approach also works in the case when the TIS sensitization is spatially inhomogeneous, as long as the SPC of each pixel is measured and applied in the conversion to the image of T . Details of T map conversion in this case are described in fig. S10.

The twin heaters in Fig. 4D are made from two small tungsten wires separated by 1 mm. The heaters are attached on a 2-mm-thick and 2 cm by 2 cm large paper board substrate (white block in the figure). A few layers of 0.5 cm by 1 cm large black carbon tapes are then stacked on the top of the heaters, with a total thickness of ~1 mm (gray block in the figure). The emissivity of the top layer is 0.90 to 0.95.

The improvement of experimental sensitivity can be experimentally extracted from the converted T map by analyzing the size of artificial step features. For example, in the line profile crossing the centers of the two heaters in Fig. 2E, the two lobes of the heaters are indistinguishable, because the difference between the temperatures at the two peak points and the center dip is smaller than the experimental sensitivity of the camera (~45 mK). In contrast, sensitizing with TIS results in a reduction in the system's sensitivity by 15 times down to ~3 mK, thus making it possible to resolve the twin heaters. Therefore, the application of TIS, which much reduces the NEDT, also contributes to the improvement of spatial resolution (D_r), especially in cases where the temperature gradient on the surface of object (∇T) is small, following a simplified equation as below

$$D_r = D_{r,c} + \text{NEDT} / |\nabla T|$$

In which $D_{r,c}$ is the instrumentally limited spatial resolution of the camera.

Demonstration of electronic imaging

As a fast, convenient, and nondestructive detection method, thermography is widely used in imaging thermal profiles of electronics, including tests for thermal-via structures (19), screening of voids at thermal interfaces (31), failure analysis in electronics packaging (32), reliability estimation of PCBs (20), and investigation of lateral electronic inhomogeneities (21).

In the weak electrical heating demonstration (fig. S11), the chip was a TS3A44159 quad single-pole double-throw analog switch with two controls (Texas Instruments). The current was applied from the COM1 terminal to the NC1 terminal at on-state of this channel. For optimal demonstration, the background IR image without the applied current was subtracted from the one with current, which generates images of ΔT_{IR} caused by joule heating.

The oEA (Fig. 3A) was performed on the processor unit of an Arduino Mega 2560 development board. In different modes characterized by IR imaging, the processor unit reads temperature data and exports terminal voltages at various frequency, which is 0 Hz for the standby mode, 250 Hz for the low-frequency mode, 500 Hz for the medium-frequency mode, and 1000 Hz for the high-frequency mode. For all conditions, there was a background thermal feature, probably arising from the background operation (including power supply, clocking, etc.) of the processor unit. A correlation of the peak IR temperature at the processor surface and the reading/exporting frequency is shown in fig. S12.

The quantitative oEA (Fig. 3, B and C) was performed on a PCB with parallel circuit traces purchased from Uxcell. A finite-element analysis using the heat transfer module of COMSOL Multiphysics was developed to simulate the surface thermal profile at different current inputs. The surrounding air temperature (influenced by the cold plate) was calibrated on the basis of the thermal profile of a single circuit trace with current from 0.4 to 1.1 A. The model was then applied to map the currents in three traces with different experiment setups, which were then compared with the actual currents flowing in the circuit traces. Detailed information of the modeling can be found in figs. S13 to S15. As an additional benefit, the coverage of TIS can eliminate the effect of emissivity variation across the object surface in thermal imaging, which is typical for PCBs.

Experimental details for *in vivo* tumor growth

RMA cells were cultured in RPMI 1640 (Thermo Fisher Scientific) and B16-F10 cells (obtained from University of California, Berkeley, Cell Culture Facility) were cultured in Dulbecco's modified Eagle's medium (Thermo Fisher Scientific). In all cases, media contained 5% fetal bovine serum (Omega Scientific), glutamine (0.2 mg/ml; Sigma Aldrich), penicillin (100 U/ml; Thermo Fisher Scientific), streptomycin (100 µg/ml; Thermo Fisher Scientific), gentamycin sulfate (10 µg/ml; Lonza), 50 µM β-mercaptoethanol (EMD Biosciences), and 20 mM Hepes (Thermo Fisher Scientific), and the cells were cultured in 5% CO₂.

For tumor growth experiments, RMA or B16-F10 cells were washed and resuspended in phosphate-buffered saline (Thermo Fisher Scientific) and injected subcutaneously into the belly of C57BL/6J mice (originally obtained from the Jackson laboratory) at a dose of ~10⁵ cells in a total volume of 50 µl per injection site. The tumor growth was monitored daily.

Note that as opposed to the hypervascularity around the natural cancer cells for human, the artificially introduced tumors in mice

typically have impaired blood supplies, mainly because of the much faster growth rate of these tumors and the immunodeficiency of laboratory mice, causing a slightly lower local temperature, instead of higher as in the case of human.

Besides cancer screening, IR imaging of blood vessels is also critical for intravascular sampling of venous blood, intravenous injections of drug solutions (33), monitor of health parameters such as blood pressure (34), and diagnostics of circulatory disorders (35). This requirement can also be readily met with the millikelvin sensitivity enabled by TIS, which shows a clear improvement in the imaging of cephalic veins (fig. S17). We note that the scope of TIS application goes much beyond the limited cases demonstrated in this work and can be extended to most areas of medical thermography, including checking of musculoskeletal disorders (36), diagnosis of rheumatic diseases (37), dermatological applications (38), evaluation of transplantation (39), and imaging of brain activities (40).

SUPPLEMENTARY MATERIALS

Supplementary material for this article is available at <http://advances.sciencemag.org/cgi/content/full/6/50/eabd8688/DC1>

REFERENCES AND NOTES

1. F. Niklaus, C. Vieider, H. Jakobsen, MEMS-based uncooled infrared bolometer arrays: A review, in *Photonics Asia 2007* (SPIE, 2008), vol. 6836.
2. E. Mounier, Technical and market trends for microbolometers for thermography and night vision, in *SPIE Defense, Security, and Sensing* (SPIE, 2011), vol. 8012.
3. A. Rozloznik, Bringing up-to-date applications of infrared thermography to surveillance, safety, and rescue, in *AeroSense 2000* (SPIE, 2000), vol. 4020.
4. X. Lu, G. Liao, Z. Zha, Q. Xia, T. Shi, A novel approach for flip chip solder joint inspection based on pulsed phase thermography. *NDT&E Int.* **44**, 484–489 (2011).
5. B. B. Lahiri, S. Bagavathiappan, T. Jayakumar, J. Philip, Medical applications of infrared thermography: A review. *Infrared Phys. Technol.* **55**, 221–235 (2012).
6. C.-C. Cheng, T.-M. Cheng, C.-H. Chiang, Defect detection of concrete structures using both infrared thermography and elastic waves. *Autom. Constr.* **18**, 87–92 (2008).
7. V. Mouillet, J. Lamontagne, F. Durrieu, J.-P. Planche, L. Lapalu, Infrared microscopy investigation of oxidation and phase evolution in bitumen modified with polymers. *Fuel* **87**, 1270–1280 (2008).
8. A. Voshell, N. Dhar, M. Rana, Materials for microbolometers: Vanadium oxide or silicon derivatives, in *SPIE Commercial + Scientific Sensing and Imaging* (SPIE, 2017), vol. 10209.
9. C. Li, G. D. Skidmore, C. Howard, C. J. Han, L. Wood, D. Peysha, E. Williams, C. Trujillo, J. Emmett, G. Robas, D. Jardine, C.-F. Wan, E. Clarke, Recent development of ultra small pixel uncooled focal plane arrays at DRS, in *Defense and Security Symposium* (SPIE, 2007), vol. 6542.
10. M. Kohin, N. Butler, Performance limits of uncooled VOx microbolometer focal plane arrays, in *Defense and Security* (SPIE, 2004), vol. 5406.
11. A. Rogalski, Next decade in infrared detectors, in *SPIE Security + Defence* (SPIE, 2017), vol. 10433.
12. R. J. Thorn, O. C. Simpson, Spectral emissivities of graphite and carbon. *J. Appl. Phys.* **24**, 633–639 (1953).
13. F. J. Morin, Oxides which show a metal-to-insulator transition at the Neel temperature. *Phys. Rev. Lett.* **3**, 34–36 (1959).
14. S. Lee, K. Hippalgaonkar, F. Yang, J. Hong, C. Ko, J. Suh, K. Liu, K. Wang, J. J. Urban, X. Zhang, C. Dames, S. A. Hartnoll, O. Delaire, J. Wu, Anomalously low electronic thermal conductivity in metallic vanadium dioxide. *Science* **355**, 371–374 (2017).
15. K. Tang, X. Wang, K. Dong, Y. Li, J. Li, B. Sun, X. Zhang, C. Dames, C. Qiu, J. Yao, J. Wu, A thermal radiation modulation platform by emissivity engineering with graded metal-insulator transition. *Adv. Mater.* **32**, 1907071 (2020).
16. M. A. Kats, R. Blanchard, S. Zhang, P. Genevet, C. Ko, S. Ramanathan, F. Capasso, Vanadium dioxide as a natural disordered metamaterial: Perfect thermal emission and large broadband negative differential thermal emittance. *Phys. Rev. X* **3**, 041004 (2013).
17. A. S. Barker, H. W. Verleur, H. J. Guggenheim, Infrared optical properties of vanadium dioxide above and below the transition temperature. *Phys. Rev. Lett.* **17**, 1286–1289 (1966).
18. J. Agassi, The Kirchhoff-Planck radiation law. *Science* **156**, 30–37 (1967).
19. R. Schacht, B. Wunderle, D. May, M. Abo Ras, W. Faust, B. Michel, H. Reichl, paper presented at the 2008 2nd Electronics System-Integration Technology Conference, Greenwich, UK, 1 to 4 September 2008.
20. A. Stoyanova, B. Bonev, N. Brayanov, paper presented at the 2018 41st International Spring Seminar on Electronics Technology (ISSE), Zlatibor, Serbia, 16 to 20 May 2018.
21. O. Breitenstein, M. Langenkamp, Lock-in contact thermography investigation of lateral electronic inhomogeneities in semiconductor devices. *Sens. Actuator A Phys.* **71**, 46–50 (1998).
22. E. Y. K. Ng, E. C. Kee, Advanced integrated technique in breast cancer thermography. *J. Med. Eng. Technol.* **32**, 103–114 (2008).
23. B. B. Lahiri, S. Bagavathiappan, B. Raj, J. Philip, Infrared thermography for detection of diabetic neuropathy and vascular disorder in *Application of Infrared to Biomedical Sciences*, E. Y. K. Ng, M. Etehadtavakol, Eds. (Springer Singapore, Singapore, 2017), pp. 217–247.
24. D. Bitar, A. Goubar, J. C. Desenclos, International travels and fever screening during epidemics: A literature review on the effectiveness and potential use of non-contact infrared thermometers. *Euro Surveill.* **14**, 19115 (2009).
25. H. Fikackova, E. Ekberg, Can infrared thermography be a diagnostic tool for arthralgia of the temporomandibular joint? *Oral Surg. Oral Med. Oral Pathol. Oral Radiol. Endod.* **98**, 643–650 (2004).
26. H. E. John, V. Niumsawatt, W. M. Rozen, I. S. Whitaker, Clinical applications of dynamic infrared thermography in plastic surgery: A systematic review. *Gland Surg.* **5**, 122–132 (2016).
27. N. Arora, D. Martins, D. Ruggerio, E. Tousimis, A. J. Swistel, M. P. Osborne, R. M. Simmons, Effectiveness of a noninvasive digital infrared thermal imaging system in the detection of breast cancer. *Am. J. Surg.* **196**, 523–526 (2008).
28. S. G. Kandlikar, I. Perez-Raya, P. A. Raghupathi, J. Gonzalez-Hernandez, D. Dabdeen, L. Medeiros, P. Phatak, Infrared imaging technology for breast cancer detection – Current status, protocols and new directions. *Int. J. Heat Mass Transf.* **108**, 2303–2320 (2017).
29. E. Y. Ng, N. M. Sudharsan, Numerical computation as a tool to aid thermographic interpretation. *J. Med. Eng. Technol.* **25**, 53–60 (2001).
30. E. Bauer, E. Pavón, E. Oliveira, C. H. F. Pereira, Facades inspection with infrared thermography: Cracks evaluation. *J. Build. Pathol. Rehab.* **1**, 2 (2016).
31. A. Gupta, L. Yongmei, N. Zamora, T. Paddock, paper presented at the *Thermal and Thermomechanical Proceedings 10th Intersociety Conference on Phenomena in Electronics Systems*, San Diego, CA, USA, 30 May to 2 June 2006.
32. D. May, B. Wunderle, R. Schacht, B. Michel, paper presented at 2012 13th International Thermal, Mechanical and Multi-Physics Simulation and Experiments in Microelectronics and Microsystems, Cascais, Portugal, 16 to 18 April 2012.
33. A. L. Urakov, A. A. Kasatkin, N. A. Urakova, Change in local temperature of venous blood and venous vessel walls as a basis for imaging superficial veins during infrared phlebography using temperature-induced tissue contrasting in *Application of Infrared to Biomedical Sciences*, E. Y. K. Ng, M. Etehadtavakol, Eds. (Springer Singapore, Singapore, 2017), pp. 429–436.
34. R. De Cesaris, A. Grimaldi, M. Balestrazzi, G. Ranieri, R. Chiarappa, F. Avantaggiato, Changes in blood pressure and thermographic values resulting from use of a beta-blocker plus diuretic and of an alpha-beta-blocker plus diuretic. *Drugs Exp. Clin. Res.* **11**, 725–729 (1985).
35. S. Bagavathiappan, T. Saravanan, J. Philip, T. Jayakumar, B. Raj, R. Karunanithi, T. M. R. Panicker, M. P. Korath, K. Jagadeesan, Infrared thermal imaging for detection of peripheral vascular disorders. *J. Med. Phys.* **34**, 43–47 (2009).
36. B. Flores, O. Susarrey, A. Yoguez, C. Gutierrez, J. Jimenez, Preliminary study on the evaluation of musculoskeletal risk of static-cycling instructors using infrared thermography, in *Advances in Ergonomics Modeling, Usability & Special Populations*, M. Soares, C. Falcão, T. Z. Ahram, Eds. (Springer International Publishing, Cham, 2017), pp. 567–574.
37. L. F. Cherkas, L. Carter, T. D. Spector, K. J. Howell, C. M. Black, A. J. MacGregor, Use of thermographic criteria to identify Raynaud's phenomenon in a population setting. *J. Rheumatol.* **30**, 720–722 (2003).
38. A. Di Carlo, Thermography and the possibilities for its applications in clinical and experimental dermatology. *Clin. Dermatol.* **13**, 329–336 (1995).
39. H. Kopsa, W. Czech, P. Schmidt, J. Zazgornik, P. Pils, P. Balcke, Use of thermography in kidney transplantation: Two year follow up study in 75 cases. *Proc. Eur. Dial. Transplant Assoc.* **16**, 383–387 (1979).
40. N. Dolensek, D. A. Gehrlach, A. S. Klein, N. Gogolla, Facial expressions of emotion states and their neuronal correlates in mice. *Science* **368**, 89–94 (2020).
41. G. Kain, M. C. Barbu, S. Hinterreiter, K. Richter, A. Petutschnigg, Using bark as a heat insulation material. *BioResources* **8**, 3718–3731 (2013).
42. A. Boudenne, L. Ibos, M. Fois, J. C. Majesté, E. Géhin, Electrical and thermal behavior of polypropylene filled with copper particles. *Compos. Part A Appl. Sci. Manuf.* **36**, 1545–1554 (2005).
43. X. Chen, M. An, R. Guo, N. Tang, Z. Peng, H. Feng, X. Li, J. Zang, N. Yang, Enhancement of thermal conductivity of polyvinyl alcohol membrane using nano-fiber. *MRS Adv.* **2**, 3651–3656 (2017).

44. S.-L. Chung, J.-S. Lin, Thermal conductivity of epoxy resin composites filled with combustion synthesized h-BN particles. *Molecules* **21**, 670 (2016).

45. Y. Li, K.-J. Zhu, Y.-G. Peng, W. Li, T. Yang, H.-X. Xu, H. Chen, X.-F. Zhu, S. Fan, C.-W. Qiu, Thermal meta-device in analogue of zero-index photonics. *Nat. Mater.* **18**, 48–54 (2019).

46. F. Sarvar, N. J. Poole, P. A. Witting, PCB glass-fibre laminates: Thermal conductivity measurements and their effect on simulation. *J. Electron. Mater.* **19**, 1345–1350 (1990).

47. T. Kim, B.-I. Choi, Y.-S. Han, K. H. Do, Feasibility study of long-wave infrared thermometry technique for simultaneous temperature and heat flux measurement. *High Temp. High Press.* **48**, 37–57 (2019).

48. R. Cabrera, E. Merced, N. Sepúlveda, Performance of electro-thermally driven VO_2 -based MEMS actuators. *J. Microelectromech. Syst.* **23**, 243–251 (2014).

49. J.-P. Bourgoin, G.-G. Allogho, A. Haché, Thermal conduction in thin films measured by optical surface thermal lensing. *J. Appl. Phys.* **108**, 073520 (2010).

50. Y. Iwasaki, paper presented at the 2008 International Conference on Wavelet Analysis and Pattern Recognition, Hong Kong, China, 30 to 31 August 2008.

51. M. San-Juan, Ó. Martín, B. J. Mirones, P. De Tiedra, Assessment of efficiency of windscreen demisting systems in electrical vehicles by using IR thermography. *Appl. Therm. Eng.* **104**, 479–485 (2016).

52. P. Bouteille, G. Legros, H. Walaszek, J. L. Bodnar, Non-destructive testing of metallic materials using passive and active infrared thermography. *Mech. Ind.* **15**, 313–321 (2014).

53. S. Bagavathiappan, B. B. Lahiri, T. Saravanan, J. Philip, T. Jayakumar, Infrared thermography for condition monitoring – A review. *Infrared Phys. Technol.* **60**, 35–55 (2013).

54. T. Omar, M. L. Nehdi, Remote sensing of concrete bridge decks using unmanned aerial vehicle infrared thermography. *Automat. Constr.* **83**, 360–371 (2017).

55. X. Li, B. Gao, W. L. Woo, G. Y. Tian, X. Qiu, L. Gu, Quantitative surface crack evaluation based on eddy current pulsed thermography. *IEEE Sens. J.* **17**, 412–421 (2016).

56. M. B. Dufour, D. Derome, R. Zmeureanu, Analysis of thermograms for the estimation of dimensions of cracks in building envelope. *Infrared Phys. Technol.* **52**, 70–78 (2009).

57. E. Grinzato, G. Cadelano, P. Bison, Moisture map by IR thermography. *J. Mod. Opt.* **57**, 1770–1778 (2010).

58. M. Alejandro, G. Romero, J. M. Sabater, J. R. Díaz, Infrared thermography as a tool to determine teat tissue changes caused by machine milking in Murciano-Granadina goats. *Livest. Sci.* **160**, 178–185 (2014).

59. C. Jang, S. Jalapu, M. Thuzar, P. W. Law, S. Jeavons, J. L. Barclay, K. K. Y. Ho, Infrared thermography in the detection of brown adipose tissue in humans. *Physiol. Rep.* **2**, e12167 (2014).

60. F. F. Farkhani, F. A. Mohammadi, paper presented at the Proceedings of 2010 IEEE International Symposium on Circuits and Systems, Paris, France, 30 May to 2 June 2010.

61. Z. Xu, T. Shi, X. Lu, G. Liao, Using active thermography for defects inspection of flip chip. *Microelectron. Reliab.* **54**, 808–815 (2014).

62. D. May, B. Wunderle, M. A. Ras, W. Faust, A. Gollhard, R. Schacht, B. Michel, paper presented at the 2008 14th International Workshop on Thermal Investigation of ICs and Systems, Rome, Italy, 24 to 26 September 2008.

63. G. Kucsko, P. C. Maurer, N. Y. Yao, M. Kubo, H. J. Noh, P. K. Lo, H. Park, M. D. Lukin, Nanometre-scale thermometry in a living cell. *Nature* **500**, 54–58 (2013).

64. F. Niklaus, C. Vieider, H. Jakobsen, Uncooled microbolometers at DRS and elsewhere through 2013, in *Image Sensing Technologies: Materials, Devices, Systems, and Applications* (SPIE, 2014), vol. 9100.

65. Y. Cui, Y. Ke, C. Liu, Z. Chen, N. Wang, L. Zhang, Y. Zhou, S. Wang, Y. Gao, Y. Long, Thermochromic VO_2 for energy-efficient smart windows. *Joule* **2**, 1707–1746 (2018).

66. N. Wang, M. Duchamp, C. Xue, R. E. Dunin-Borkowski, G. Liu, Y. Long, Single-crystalline W-doped VO_2 nanobeams with highly reversible electrical and plasmonic responses near room temperature. *Adv. Mater. Interfaces* **3**, 1600164 (2016).

67. H. H. Li, Refractive index of alkaline earth halides and its wavelength and temperature derivatives. *J. Phys. Chem. Ref. Data* **9**, 161–290 (1980).

Acknowledgments: The $\text{W}_x\text{V}_{1-x}\text{O}_2$ films were grown using the pulsed laser deposition system in the Electronic Materials Program in the Lawrence Berkeley National Laboratory, which is supported by the Director, Office of Science, Office of Basic Energy Sciences, Materials Sciences and Engineering Division, of the U.S. Department of Energy under contract no. DE-AC02-05CH11231. We are grateful to C. Dames for critical reading and discussion. IRB and/or IACUC guidelines were followed with human or animal subjects. **Funding:** This work was supported by U.S. NSF grant no. DMR-1608899. J.W. acknowledges support from the Bakar Fellowship. J.Y. acknowledges US-NSF under the grant no. 1555336. C.-W.Q. acknowledged the financial support by Ministry of Education, Republic of Singapore (grant no. R-263-000-E19-114). J.Y. acknowledges support by the U.S. National Science Foundation under grant no. 1555336.

Author contributions: J.W. conceived the project. J.W., K.T., and K.D. designed the experiments. K.T. prepared the materials and fabricated the devices. K.T. and K.D. performed the device characterization and application demonstrations. K.D. performed simulations for the performance prediction and oEA. C.J.N. and D.H.R. provided key assistance for the medical thermography experiments. J.L. helped with preparation of the figures and setup of experiments. S.L. helped with SEM imaging of the devices. Y.L. provided valuable inspiration to the project. All authors contributed to discussing the data and editing the manuscript.

Competing interests: K.T., K.D., and J.W. are inventors of a provisional patent application related to this work (No. 43/094,703, filed October 21, 2020). The authors declare that they have no competing interests. **Data and materials availability:** All data needed to evaluate the conclusions in the paper are present in the paper and/or the Supplementary Materials. Additional data related to this paper may be requested from the authors.

Submitted 17 July 2020

Accepted 20 October 2020

Published 9 December 2020

10.1126/sciadv.abd8688

Citation: K. Tang, K. Dong, C. J. Nicolai, Y. Li, J. Li, S. Lou, C.-W. Qiu, D. H. Raulet, J. Yao, J. Wu, Millikelvin-resolved ambient thermography. *Sci. Adv.* **6**, eabd8688 (2020).